

## Self-assembling properties of a series of homologous ester-diamides – from ribbons to nanotubes†

Cite this: DOI: 10.1039/c3sm51369f

François-Xavier Simon,<sup>a</sup> Thi Thanh Tam Nguyen,<sup>a</sup> Nancy Díaz,<sup>a</sup> Marc Schmutz,<sup>a</sup> Bruno Demé,<sup>b</sup> Jacques Jestin,<sup>c</sup> Jérôme Combet<sup>\*a</sup> and Philippe J. Mésini<sup>\*ad</sup>

We have studied the aggregation properties of a series of compounds BHPB-*n* bearing two amide groups and an ester alkyl chain. The number (*n*) of carbon atoms in this alkyl chain has been varied from 5 to 16. These compounds form gels at low concentration in alkanes. The gel concentrations and the heats of formation of the gels, measured by DSC, are divided into three different regimes:  $n \leq 7$ ,  $8 \leq n \leq 12$  and  $n \geq 13$ . Freeze fracture TEM shows that all the compounds self-assemble into high aspect ratio objects, *i.e.* flat ribbons for  $n \leq 7$  and irregular helical ribbons for  $n \geq 13$ . For  $8 \leq n \leq 12$ , the compounds form tubes (except BHPB-11) and were studied by SANS. The outer and inner diameter distributions of the tubes were determined from the scattered intensities with a model of paired tubes. The diameters are controlled by the length of the ester chain (*n*) and vary from 21 for BHPB-8 to 32 nm for BHPB-12 (outer diameters). The SANS measurements also provide an estimate of the ratio of paired tubes and the proportion of non-tubular objects that eventually co-exist with these tubes. Variable temperature FTIR and DSC proved that H-bonds between the amide groups are involved in all types of self-assemblies. In addition, FTIR spectra of helical tapes and nanotubes exhibit a double ester  $\nu_{\text{CO}}$  band whereas flat tapes display a single band, which confirms the involvement of the ester in the self-assemblies.

Received 15th May 2013

Accepted 8th July 2013

DOI: 10.1039/c3sm51369f

[www.rsc.org/softmatter](http://www.rsc.org/softmatter)

### Introduction

Self-assembly is an effective tool to produce nano-objects with well-defined shapes and controlled sizes. This is illustrated by the formation of nanotubes: a few compounds can form such structures simply by spontaneous self-association.<sup>1</sup> The diameters of the resulting tubes depend on the nature of the molecule and range from 10 to 500 nm. Due to their unique shape and their high aspect ratio, these nanotubes find applications for instance as scaffolds for cell growth,<sup>2</sup> as supports for 2-D crystallization of proteins<sup>3–5</sup> or as templates to form silica nanotubes<sup>6–8</sup> and mesopores in organic matrices.<sup>9</sup> They also have triggered much theoretical research by physicists to understand the mechanism of their self-assembly.<sup>10–17</sup> These studies provide models where the chirality of the constitutive molecules induces an intrinsic bending of the self-assembled layers and yields both helical and tubular shapes. These models explain for instance

how an enantiomeric excess of chiral counterions control the diameters of the self-assembled tubules formed from gemini surfactants.<sup>18</sup> However they cannot explain the few examples of non-chiral molecules forming nanotubes.<sup>19,20</sup> These models also rely on a phenomenological description of the elastic energy but do not take into account the local packing or interactions between the molecules and thus cannot identify the molecular parameters that govern the formation of the tubes. Resolution of the structures unveiling interactions at a molecular level has been achieved only in a few cases, where the objects have been successfully ordered.<sup>21,22</sup> But generally these size-limited objects give diffuse signals on selected area diffraction and powder patterns in solution. As a result, one lacks predictability to control the shape and the diameters of those self-assemblies. Many efforts have been made to tune the size of self-assembled nanotubes. It has been achieved by addition of salts in the case of tubes formed from gemini surfactants.<sup>23</sup> For other systems, the molecular parameters controlling the diameters have been successfully identified, *e.g.* the relative size of the polar heads in a series of bolaphiles,<sup>24</sup> the nature of the polar group in glycerolipids<sup>25</sup> or the amino-acid residues in peptidic nanotubes.<sup>26</sup> However, these examples are very rare and modification of a given self-assembling compound most often precludes the formation of nanotubes.

We have shown previously that 3,5-bis-(5-hexylcarbamoyl-pentyloxy)-benzoic acid decyl ester (BHPB-10, Fig. 1,  $n = 10$ ) was able to self-associate to form nanotubes in alkanes.<sup>27</sup>

<sup>a</sup>Centre National de la Recherche Scientifique, Institut Charles Sadron, 23 rue du Loess, BP 84047, F-67034, Strasbourg, France. E-mail: mesini@ics-cnrs.unistra.fr; combat@ics-cnrs.unistra.fr; Fax: +33 3 88 41 40 99; Tel: +33 3 88 41 40 70

<sup>b</sup>Institut laue Langevin, 6 rue Horowitz, BP 156, F-38042, Grenoble, France

<sup>c</sup>Laboratoire Léon Brillouin, Bât. 563 CEA Saclay, 91191 Gif sur Yvette, France

<sup>d</sup>International Center for Frontier Research in Chemistry, 8 allée Gaspard Monge, F-67083, Strasbourg, France

† Electronic supplementary information (ESI) available: Characterization data of all synthesized compounds; best fits for all the compounds in log-log, Kratky and Porod representation. See DOI: 10.1039/c3sm51369f

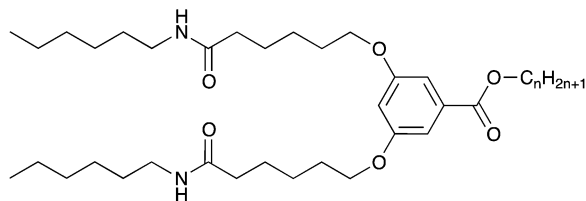


Fig. 1 Structure of BHPB-*n*.

Herein we have studied the properties of a series of analogues where the length of the ester chain has been varied. When the length remains within a certain range, these analogues yield tubes with controlled diameters as shown by SANS. When this length goes beyond this range, the compounds self-assemble into either flat or helical tapes. The morphology of the self-assemblies in the whole series has been explored by freeze-fracture TEM. The interactions that govern the self-assemblies have been studied by FTIR and DSC.

## Material and methods

### Compounds

The chemicals were purchased from Aldrich or Acros and used as received. NMR spectra were recorded on a Bruker Avance 400 operating at 400 MHz for  $^1\text{H}$  and 100 MHz for  $^{13}\text{C}$ . The FTIR spectra of the neat compounds were recorded on a Bruker Vertex 70 spectrometer equipped with an ATR diamond reflection unit (MVPStar). Mass spectra were recorded with a Bruker Daltonique microTOF operating with an electrospray source.

The compounds were synthesized according to Scheme 1.

As an example, the synthesis and characterization of DHB-5 and BHPB-5 are given below. The data on the characterization of all other compounds are given in ESI.†

**Pentyl-3,5-dihydroxybenzoate (DHB-5).** A solution of 3,5-dihydroxybenzoic acid (5 g, 32.4 mmol), pentanol (2.85 g, 32.4 mmol, 1 equiv.) and *para*-toluenesulfonic acid (279 mg, 1.62 mmol, 0.05 equiv.) in toluene (150 mL) was refluxed in a Dean–Stark apparatus. After elimination of water, the reaction mixture was cooled to 25 °C and the toluene was evaporated under reduced pressure to afford a yellow oil that was mixed with aqueous saturated  $\text{NaHCO}_3$  (500 mL). The resulting mixture was extracted with  $\text{CH}_2\text{Cl}_2$  ( $3 \times 50$  mL). The combined

organic phases were dried ( $\text{Na}_2\text{SO}_4$ ), filtered and evaporated under reduced pressure. The residue was chromatographed ( $\text{SiO}_2$ ,  $\text{MeOH}/\text{CH}_2\text{Cl}_2$ : 5/95 eluent) to afford pure DHB-5 as a colorless oil (5.74 g, yield 79%).  $^1\text{H}$  NMR (400 MHz,  $\text{CDCl}_3$ ):  $\delta$  [ppm] 7.01 (d, 2H,  $J = 1.8$  Hz, C2-*H*, C6-*H*), 6.98 (s large, 2H, O-*H*), 6.60 (t, 1H,  $J = 2.0$  Hz, C4-*H*), 4.30 (t, 2H,  $J = 6.5$  Hz,  $\text{COOCH}_2$ ), 1.76 (m, 2H,  $\text{COOCH}_2\text{CH}_2$ ), 1.36 (m, 4H,  $\text{COOCH}_2\text{CH}_2(\text{CH}_2)_2$ ), 0.90 (t, 3H,  $J = 6.5$  Hz,  $\text{CH}_3$ ).  $^{13}\text{C}$  NMR (100 MHz,  $\text{CDCl}_3$ ):  $\delta$  [ppm] 167.5 (COO), 156.8 (C3, C5), 132.1 (C1), 108.9 (C2, C6), 107.3 (C4), 66.1 ( $\text{COOCH}_2$ ), 28.2 ( $\text{COOCH}_2\text{CH}_2$ ), 22.1 ( $\text{COO}(\text{CH}_2)_2\text{CH}_2$ ), 22.6 ( $\text{COO}(\text{CH}_2)_3\text{CH}_2$ ), 14.0 ( $\text{CH}_3$ ); FTIR (ATR-diamond)  $\nu_{\text{max}}$ : 3351, 2958, 2933, 2873, 1763, 1749, 1688, 1599  $\text{cm}^{-1}$ ; HRMS (FAB+)  $m/z$  225.1118 ( $\text{MH}^+$ , calcd for  $\text{C}_{12}\text{H}_{16}\text{O}_4$ : 225.1121). Anal. found C, 63.76; H 7.27. Calcd for  $\text{C}_{12}\text{H}_{16}\text{O}_4$ : C, 64.27; H 7.19.

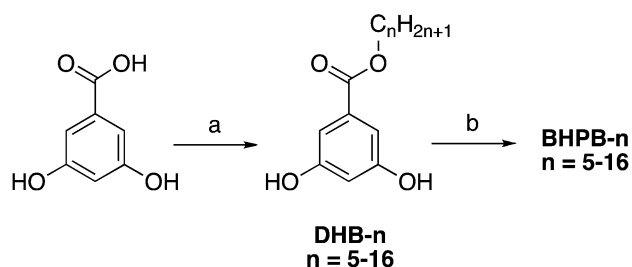
**3,5-Bis-(5-hexylcarbamoyl-pentoxyl)-benzoic acid pentyl ester (BHPB-5).** A solution of pentyl-3,5-dihydroxybenzoate (204 mg, 0.91 mmol, 1 equiv.), 6-bromo-*N*-hexylhexanamide<sup>27</sup> (509 mg, 1.83 mmol, 2.05 equiv.) and  $\text{Bu}_4\text{NBr}$  (115 mg, 0.36 mmol, 0.4 equiv.) in DMF (50 mL) was treated with  $\text{K}_2\text{CO}_3$  (625 mg, 4.52 mmol, 5 equiv.) and stirred at 50 °C for 12 h. The mixture was combined with water (200 mL) and acidified to pH 1 to 2 with aqueous HCl (10%). The precipitate was filtered and recrystallized in acetonitrile to afford pure BHPB-5 as a white solid (473 mg, 84%); M.p. 82.5 °C.  $^1\text{H}$  NMR (400 MHz,  $\text{CDCl}_3$ ):  $\delta$  [ppm] 7.14 (d, 2H,  $J = 2.2$  Hz, C2-*H*, C6-*H*), 6.60 (t, 1H,  $J = 2.2$  Hz, C4-*H*), 5.44 (s broad, 2H, NH), 4.29 (t, 2H,  $J = 6.7$  Hz,  $\text{COOCH}_2$ ), 3.97 (t, 4H,  $J = 6.5$  Hz,  $\text{ArOCH}_2$ ), 3.24 (q, 4H,  $J = 6.7$  Hz,  $\text{CH}_2\text{NHCO}$ ), 2.19 (t, 4H,  $J = 7.6$  Hz,  $\text{CH}_2\text{CONH}$ ), 1.76 (m, 10H,  $\text{COOCH}_2\text{CH}_2$ ,  $\text{ArOCH}_2\text{CH}_2$ ,  $\text{ArOCH}_2\text{CH}_2\text{CH}_2$ ), 1.53–1.29 (m, 24H,  $\text{CH}_2$ ), 0.88 (t, 9H,  $J = 6.8$  Hz,  $\text{CH}_3$ ).  $^{13}\text{C}$  NMR (100 MHz,  $\text{CDCl}_3$ ):  $\delta$  [ppm] 172.7 (CONH), 166.5 (COO), 160.0 (C3, C5), 132.3 (C1), 107.7 (C2, C6), 106.2 (C4), 68.0 ( $\text{ArOCH}_2$ ), 65.3 ( $\text{COOCH}_2$ ), 39.5 ( $\text{CH}_2\text{NH}$ ), 36.7 ( $\text{CH}_2\text{CONH}$ ), 31.4 ( $\text{NH}(\text{CH}_2)_3\text{CH}_2$ ), 29.6 ( $\text{NHCH}_2\text{CH}_2$ ), 28.9 ( $\text{ArOCH}_2\text{CH}_2$ ), 28.1 ( $\text{COOCH}_2\text{CH}_2$ ), 26.6 ( $\text{NH}(\text{CH}_2)_2\text{CH}_2$ ), 25.8 ( $\text{COO}(\text{CH}_2)_2\text{CH}_2$ ), 25.7 ( $\text{CH}_2\text{CH}_2\text{CONH}$ ), 25.5 ( $\text{CH}_2(\text{CH}_2)_2\text{CONH}$ ), 22.6 ( $\text{COO}(\text{CH}_2)_3\text{CH}_2$ ), 22.5 ( $\text{NH}(\text{CH}_2)_4\text{CH}_2$ ), 14.1 ( $\text{COO}(\text{CH}_2)_4\text{CH}_3$ ), 14.0 ( $\text{NH}(\text{CH}_2)_5\text{CH}_3$ ). IR (ATR-diamond)  $\nu_{\text{max}}$ : 3292, 3093, 2952, 2926, 2857, 1718, 1638, 1611, 1552, 1443, 1318, 1230, 1159  $\text{cm}^{-1}$ . HRMS (FAB+)  $m/z$  619.4659 ( $\text{MH}^+$ , calcd for  $\text{C}_{36}\text{H}_{62}\text{N}_2\text{O}_6$ : 619.4681). Anal. found: C, 70.23; H, 10.19; N, 4.39. Calcd for  $\text{C}_{36}\text{H}_{62}\text{N}_2\text{O}_6$ : C, 69.86; H, 10.10; N, 4.53.

### Formation of the gels

BHPB-*n* (20 mg) and cyclohexane (980 mg) were weighed in a vial (diameter 14 mm). The vial was closed tightly with a screw cap equipped with a Teflon gasket. The mixture was heated at 80 °C until complete dissolution of BHPB-*n* and the solution let stand at 25 °C until the formation of a gel.

### DSC

The thermograms were measured with a microcalorimeter DSC III (Setaram) at a heating rate of 0.3 and 0.1 °C  $\text{min}^{-1}$  and gave the same peak positions. Two heating–cooling cycles were carried out. The peak integrations were done on the second heating phase for all the samples.



Scheme 1 Synthesis of compounds BHPB-*n*. (a)  $\text{C}_n\text{H}_{2n+1}\text{OH}$ , *para*-toluenesulfonic acid, toluene, 140 °C; (b)  $\text{C}_6\text{H}_{13}\text{NHCOc}_5\text{H}_{10}\text{Br}$ ,  $\text{Bu}_4\text{NBr}$ ,  $\text{K}_2\text{CO}_3$ , DMF.

## FTIR

Spectra were recorded on a Bruker Vertex 70 spectrophotometer equipped with a thermostatic cell holder and a temperature controlling unit (Specac West 6100+). The gels were placed in a NaCl cell with an optical path of 0.1 mm. The temperature was increased by 1 °C before each spectrum was obtained (rate 1 °C min<sup>-1</sup>) and the measurement was performed after the temperature was stabilized (about half a minute). The spectra were recorded at different temperatures, were corrected for CO<sub>2</sub> and water vapor and compensated for C<sub>6</sub>H<sub>12</sub>. They were processed and fitted using Igor (Wavemetrics, Inc.). The maxima of the peaks were found with the built-in algorithm using second derivatives.

## Electron microscopy

The freeze fracture was performed according to protocols previously described.<sup>28</sup> The grids were observed with a Philips CM 12 operating at 120 kV or a FEI Tecnai G2 20 Twin operating at 200 kV. The images were taken with a CCD camera. The distances were measured with the software Analysis (SIS-Olympus Münster Germany). The cross-sectional sizes of the objects were measured on statistically large numbers of objects (c.a. 400). The statistics obtained from different samples or from different freeze fractures prepared from the same compounds showed superimposable histograms.

## Small angle neutron scattering

**Experimental.** Small Angle Neutron Scattering (SANS) experiments were performed on the diffractometer D22 at the Institut Laue Langevin (Grenoble, France). Data were collected at four sample-to-detector distances:  $d = 1.5, 3.6, 11.20$  m (collimation length  $d' = 11.20$  m, wavelength  $\lambda = 6$  Å, wavelength distribution  $\Delta\lambda/\lambda = 0.1$ ) and  $d = 17.60$  m ( $d' = 17.60$  m,  $\lambda = 16$  Å,  $\Delta\lambda/\lambda = 0.1$ ). The scattered intensity was recorded with a 2-dimensional <sup>3</sup>He gas detector allowing translational offset in order to increase the highest scattering angle. These configurations allowed measurements in the  $q$  vector range 0.0011–0.64 Å<sup>-1</sup> ( $q$  is the magnitude of the scattering vector defined by  $q = 4\pi/\lambda \sin(\theta)$ , where  $\lambda$  is the wavelength of the incident beam and  $2\theta$  the scattering angle). Measurements were performed in 1 mm thick quartz cells (Helma). Deuterated cyclohexane was used as the solvent in order to increase contrast. The temperature was kept constant at 22 °C during all measurements.

Data were corrected with standard ILL programs for isotropic scattering. They were converted to an absolute scale using H<sub>2</sub>O as a standard to yield the total differential scattering cross section per unit volume  $d\Sigma_{\text{sample}}^{\text{total}}/d\Omega(q)$  (cm<sup>-1</sup>). This quantity is the sum of the coherent differential scattering cross-section of the solute  $d\Sigma_{\text{solute}}^{\text{coherent}}/d\Omega(q)$  (cm<sup>-1</sup>) related to the structure of the aggregates and a background that comprises the scattering of the solvent and the incoherent scattering of the BHPB- $n$  molecules. The latter contributions were subtracted and slightly adjusted in order to get a coherent signal very close to zero in the highest  $q$  region (around 0.5–0.6 Å<sup>-1</sup>).

**Data modeling.** The corrected scattered intensity  $d\Sigma_{\text{solute}}^{\text{coherent}}/d\Omega(q)$  (cm<sup>-1</sup>) (denoted  $d\Sigma/d\Omega(q)$  hereafter) can be compared to several models in order to determine the form and the size of the aggregates. In the case of monodispersed non-interacting particles, it can be written as

$$d\Sigma/d\Omega(q) = \phi_v \Delta\rho^2 V_P P(q) \quad (1)$$

where  $\phi_v$  is the volume fraction of the particles,  $V_P$  their volume (cm<sup>3</sup>),  $P(q)$  their normalized form factor, and  $\Delta\rho$  the difference between their scattering length density  $\rho$  (cm<sup>-2</sup>) and that of the solvent. In some gels, large heterogeneities were sometimes observed. Thus, the real volume fraction under investigation was not known with a great accuracy and we chose to normalize the data to the Porod invariant as defined by

$$Q = \frac{1}{2\pi^2} \int_0^\infty q^2 d\Sigma/d\Omega(q) dq \quad (2)$$

For an ideal two-phase system this quantity is related to the contrast factor and the volume fraction of the scattering particles through the relation

$$Q = \Delta\rho^2 \phi_v (1 - \phi_v) \quad (3)$$

Since the volume fraction is very low (around 1%),  $Q \approx \Delta\rho^2 \phi_v$ , and the normalisation to the invariant can finally be written as

$$\frac{d\Sigma/d\Omega(q)}{Q} = V_P P(q) \quad (4)$$

The Porod invariant was calculated from the integration of  $q^2 d\Sigma/d\Omega(q)$  between  $q_{\text{min}}$  and 0.4 Å<sup>-1</sup>.

**Analysis procedure.** The finite instrument resolution was evaluated from the size of the incident beam on the detector and the wavelength spread as described by Pedersen<sup>29</sup> and derived for D22 by Grillo.<sup>30</sup> Normalized data were then compared to the models (isolated infinite tubes, clusters of tubes, and combination of both, as explained in the Results and discussion section) using the IGOR Pro package and the extension developed by the NIST Center for Neutron Research.<sup>31</sup> This approach allowed the determination of the average external radius  $r_{\text{ext}}$ , the distribution width  $\Delta r_{\text{ext}}$ , the thickness of the wall of the hollow cylinders  $e$  and the fraction of tubes forming clusters  $f_{\text{cluster}}$ . A more general scaling factor (*scale*) was introduced in order to overcome problems with the Porod invariant normalization. Finally, a small background contribution (bkg) was also considered.

## Results and discussion

### Thermodynamic properties

The structure of BHPB- $n$  is depicted in Fig. 1.  $n$  is the number of carbon atoms in the ester chain. BHPB- $n$  form organogels in alkanes for  $n \geq 5$ . Compounds with smaller chain lengths form precipitates in these solvents, and have not been studied in this paper. Gels are formed simply by heating the compound in the solvent at a given wt concentration until complete dissolution

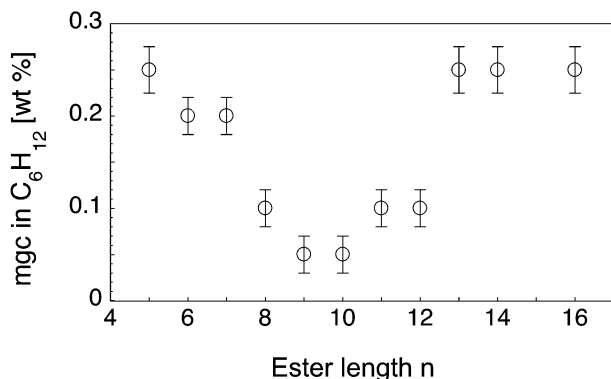


Fig. 2 Minimum gel concentrations of BHPB-*n* in cyclohexane.

and cooling the resulting solution at 25 °C. This gelation is thermoreversible, which shows that the molecules self-assembled through non-covalent interactions. The minimum gelator concentrations required to form a self-supporting gel (mgc) were measured in cyclohexane at 25 °C and are reported as a function of the ester chain length *n* (Fig. 2).

The mgc values are divided into two sets: smaller than 0.1 wt% for  $8 \leq n \leq 12$  and equal to or greater than 0.2 wt% for  $n \leq 7$  or  $n \geq 13$ . The lowest value, found for BHPB-9 and BHPB-10, is 0.05 wt%, which shows that they are efficient organogelators.<sup>32</sup> The enthalpy of the gel-to-sol transition was measured by DSC for each compound at 4 different concentrations above the gel concentration.

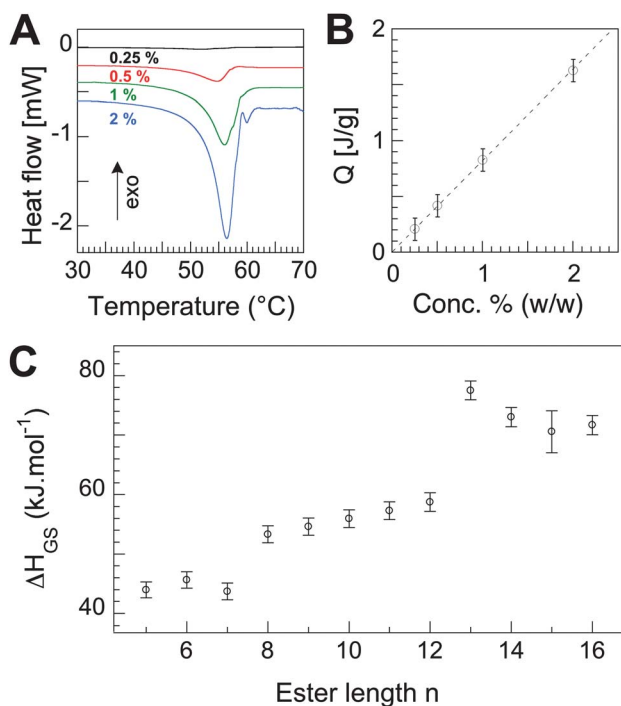


Fig. 3 (A) DSC thermograms of BHPB-12 in cyclohexane, for different concentrations (endothermic flow down); (B) measured heat per gram of gels as a function of the concentration. The dashed line gives the best linear fit and corresponds to  $\Delta H = 58.8 \pm 1.6$  kJ mol<sup>-1</sup>; (C) enthalpies of gel melting vs. the number of carbon in the ester chain.

The lowest concentration gives a weak but still detectable enthalpy value (Fig. 3A). The gel-to-sol transition temperature increases with concentration and the heat *Q* is proportional to gelator concentration (Fig. 3B), meaning that the transition enthalpy per mole of BHPB-*n*,  $\Delta H$ , is constant in the studied *C*-range. For a better accuracy,  $\Delta H$  values are derived from the linear fit of the *Q* vs. *C* plot. The plot of  $\Delta H$  values against the number *n* (Fig. 3C) clearly displays three regimes that were slightly visible for the mgc. In the first regime, when  $n \leq 7$ ,  $\Delta H$  values are below 46 kJ mol<sup>-1</sup>, in the third one, when  $n \geq 13$ , they are above 71 kJ mol<sup>-1</sup> and, in both regimes, they do not vary monotonously. In the second regime, when  $8 \leq n \leq 12$ ,  $\Delta H$  varies from 53 to 58 kJ mol<sup>-1</sup> with a linear progression. These regimes are separated by sharp gaps in enthalpy: 10 kJ mol<sup>-1</sup> for the first one and 19 kJ mol<sup>-1</sup> for the second one. These differences are much larger than the values of the melting heat per methylene in paraffins<sup>33–35</sup> (3.85 to 4.10 kJ per mol of CH<sub>2</sub>) or polyethylene<sup>34</sup> (3.97 kJ per mol of CH<sub>2</sub>). Therefore they cannot be explained by the sole van der Waals interactions of the additional methylene unit. The division into different regimes reflects a different kind of packing. Within the linear regime, the slope is  $1.14 \pm 0.47$  kJ per mole of CH<sub>2</sub>. This slight variation suggests that compounds BHPB-8 through BHPB-12 self-assemble with a very similar mechanism.

### Infrared spectroscopy

In order to identify the interactions involved in the self-assemblies, FTIR measurements were carried out on the gels. The spectrum of the gels of BHPB-10 in C<sub>6</sub>H<sub>12</sub> (2 wt%) as an example is shown in Fig. 4.

The presence of a NH-stretching band at 3299 cm<sup>-1</sup> (Fig. 4 left), an amide I band at 1642 cm<sup>-1</sup> and an amide II band at 1551 cm<sup>-1</sup> (Fig. 4 right) provides strong evidence of H-bonds between all the amide groups within the self-assemblies. By comparison, in chloroform, BHPB-10 is completely dissociated and the same bands are strongly shifted ( $\nu_{\text{NH}}$ : 3449 cm<sup>-1</sup>, amide I: 1662 cm<sup>-1</sup>, amide II: 1519 cm<sup>-1</sup>), which proves that the amide groups are not H-bonded. The spectra were recorded for all species at different temperatures. As an example, the

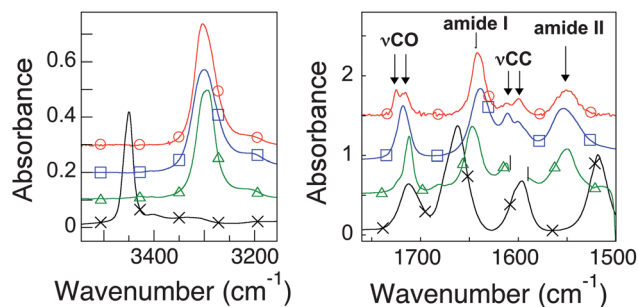


Fig. 4 FTIR spectra of BHPB-10 in C<sub>6</sub>H<sub>12</sub> (gel – 2 wt%) (○); BHPB-6 in C<sub>6</sub>H<sub>12</sub> (gel – 2 wt%) (□); BHPB-10 in toluene (gel – 2 wt%) (△) (for the sake of clarity the uncompensated peak of toluene at 1600 has been erased); BHPB-10 in CHCl<sub>3</sub> (solution – 2 wt%) (×). Left: NH stretching region. Right: CO stretching and CN bending region.

frequencies and intensity of the amide I band and  $\nu_{\text{NH}}$  bands of BHPB-8 are displayed in Fig. 5.

When the gel is heated above the transition temperature, the amide I band broadens and diminishes while a shoulder appears at 1680–1690  $\text{cm}^{-1}$  (Fig. 5A). The NH band at 3299  $\text{cm}^{-1}$  also decreases while a weak band appears at 3455  $\text{cm}^{-1}$  (Fig. 5C). These new shifts are characteristic of non-bonded amides and are indeed close to the ones in  $\text{CHCl}_3$ . Both the frequencies and the intensities of the bands show a steep variation at a temperature that coincides with the transition observed by DSC (Fig. 5B and C). It proves that H-bonds between amides are involved in the self-assemblies. The energy of such bonds can be assumed to be equal to the enthalpy of self-association of *N*-methylacetamide in aprotic solvents, 16 kJ  $\text{mol}^{-1}$ ,<sup>36</sup> multiplied by two since two amides are involved. This value represents a large part of the transition enthalpies measured by DSC (more than 50% when  $n \leq 12$ ) indicating the predominance of the H-bonds in the self-assembly.

The ester CO stretching band is split into two bands (1725 and 1716  $\text{cm}^{-1}$ ). This double frequency is observed for all species except BHPB-5 and 6. The lower frequency cannot be attributed to a H-bond from one of the amide groups since the corresponding  $\nu_{\text{NH}}$  band should be visible at 3350  $\text{cm}^{-1}$ . It may reflect the presence of two sets of molecules with different orientations or environments within the self-assemblies. Different orientations of the carboxyl group with regard to the aromatic ring can lead to different shifts for the ester mainly due to different degrees of conjugations, and may explain the double frequency also observed for the aromatic C=C stretching band (1599  $\text{cm}^{-1}$  and 1612  $\text{cm}^{-1}$ ). The amide I and the NH stretching bands, even if they appear like single bands, can

be also deconvoluted into two peaks (1644/1638  $\text{cm}^{-1}$  and 3307/3285  $\text{cm}^{-1}$  resp.). Deconvolutions with similar peak shifts can be done for all species except BHPB-5 and BHPB-6. When the temperature rises above the gel-to-sol transition, the double ester band also evolves toward a single peak (Fig. 5A). These observations prove that not only the amide groups but also the ester groups are involved in the formation of self-assemblies and justify *a posteriori* the need to modify the ester group to probe its role.

As a conclusion, both the DSC and FTIR studies show that the main interactions driving the self-assembly are the H-bonds between the amide groups. They account for half of the transition enthalpy. The splitting of some bands corroborates the involvement of the esters in the assemblies. It also suggests that the structure of the BHPB-*n* self-assemblies with  $n \geq 7$  comprises two different sets of molecules with asymmetrical orientations.

### Electron microscopy

The microscopic structure of the gels was explored by freeze fracture TEM. This technique originally developed for aqueous media has been successfully implemented in organic solvents especially to observe organogels.<sup>37–40</sup> The self-assemblies were examined by electron microscopy at different times after the formation of the gels. The same structures were observed in the gels after a few minutes or after 6 months, which shows their stability. The width or diameters of the observed objects were measured for a statistically relevant number of objects (about 400) to calculate their average values and distribution (reported in Table 1). The uncertainty is rather large (3 nm) because the replicas are obtained after coating the samples with metal particles.

We present hereafter the morphologies and the sizes of the structures in each regime as identified by DSC. When  $n \leq 7$ ,

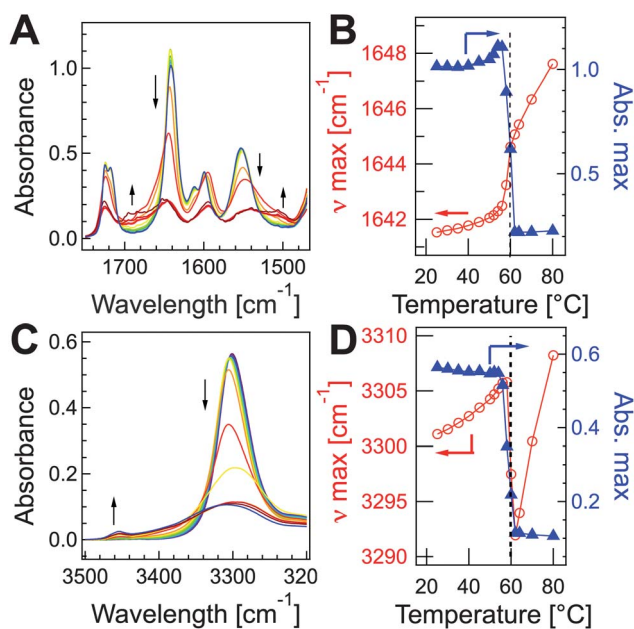


**Fig. 5** VT-FTIR spectra of gels of BHPB-8 in  $\text{C}_2\text{H}_{12}$  (2 wt%) from 25 °C to 80 °C in the CO stretching and CN bending region (A) and in the NH stretching region (C). Frequencies (○) and intensities (▲) of the amide I band (B) and of the  $\nu_{\text{NH}}$  band (D) vs. temperature. Dashed line: transition temperature measured by DSC.

**Table 1** Width or diameters of BHPB-*n* self-assemblies measured from TEM

Compound	Shape of the self-assemblies	Avg. width or diameter <sup>a</sup> [nm]	Std. deviation <sup>a</sup> [nm]
BHPB-5	Flat ribbons	70.1	23.3
BHPB-6	Flat ribbons	41.5	18.1
BHPB-7	Flat + helical ribbons	34.2	9.1
BHPB-8	Tubes	24.8	3.6
BHPB-9	Tubes	25.8	4.4
BHPB-10	Tubes	28.5	3.8
BHPB-11	Helical + twisted ribbons	32.7	7.2
BHPB-12	Tubes and ribbons	34.1	6.9
BHPB-13	Helical + twisted ribbons	56.4	19.7
BHPB-14	Helical + twisted ribbons	40.7	13.2
BHPB-15	Helical + twisted ribbons	39.5	8.4
BHPB-16	Helical + twisted ribbons	23.3	5.1

<sup>a</sup> Uncertainty  $\pm$  3 nm.

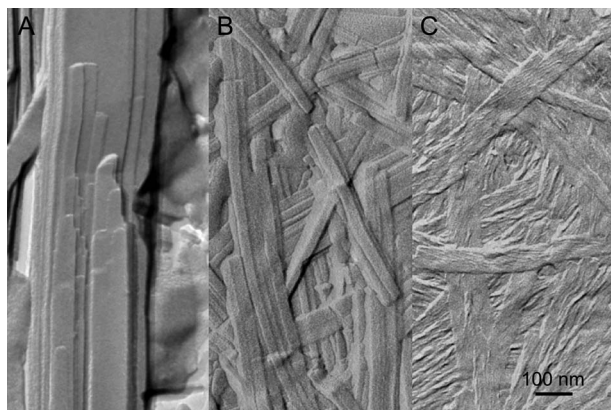


**Fig. 6** Freeze fracture TEM of BHPB-*n* in  $C_6H_{12}$  (2 wt%). (A) BHPB-5; (B) BHPB-6; (C) BHPB-7.

compounds BHPB-*n* form ribbons of several  $\mu\text{m}$  length (Fig. 6). For BHPB-5, ribbons with polydisperse widths (between 30 nm and 150 nm) stack to form thick multilamellar objects. BHPB-6 and BHPB-7 form individualized ribbons with polydisperse widths between 13 and 160 nm (average 41 nm) and between 15 and 85 nm (average 34 nm) respectively.

The subgroup of compounds BHPB-5 to 7 has a trend to form narrower and thinner objects when the ester size increases. Although BHPB-7 belongs to the same DSC regime as BHPB-5 and BHPB-6, it is distinguished by a different morphology: it forms twisted ribbons in large proportions (Fig. 6C). For  $n = 8, 9$  and 10, BHPB-*n* form regular cylinders with lengths in the range of micrometers (Fig. 7). The shadowing pattern of the visible ends of the cylinder shows that they are hollow (Fig. 7, arrows). The diameters of the tubes significantly increase when  $n$  the length of the ester chain increases. BHPB-11 forms no tubes but a mixture of irregular helical tapes with different diameters (Fig. 7D). BHPB-12 self-assembles into mixtures of tubes and helical tapes (Fig. 7E).

The mean diameter of the objects formed by BHPB-12 is  $34.1 \pm 6.9$  nm, which is larger and more polydisperse than the

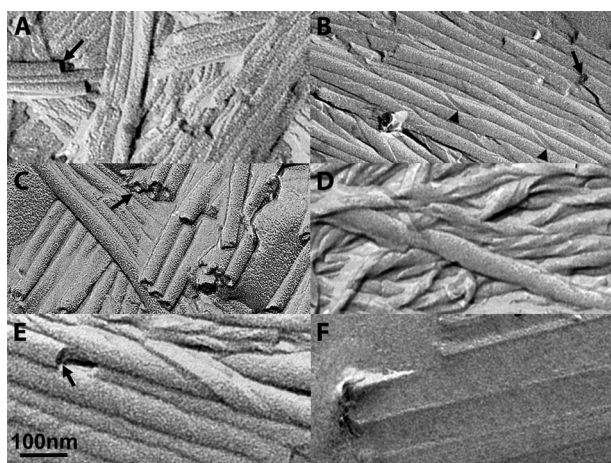


**Fig. 7** Freeze fracture TEM. (A) BHPB-8; (B) BHPB-9; (C) BHPB-10; (D) BHPB-11; (E) BHPB-12 in  $C_6H_{12}$  (2 wt%). Arrows: cross section of tube ends. Arrowheads: helical grooves. (F) BHPB-10 in toluene (4 wt%).

previous ones. Even if BHPB-8 to BHPB-10 form more regular tubes, a small proportion of them bear helical grooves (Fig. 7B, arrowheads), indicating that they stem from wound tapes. The presence of helical tapes among tubes has been observed by TEM as early as the 80s by Kunitake, who identified them as precursors of the tubes.<sup>41</sup> This hypothesis has been lately confirmed by scattering techniques.<sup>42</sup> It has also been explained by many theoretical models.<sup>10–12,14,17</sup> In toluene, BHPB-8 to BHPB-12 self-assemble with a different morphology from that in  $C_6H_{12}$ : they form only thick and straight fibrils (Fig. 7F). In addition, the FTIR spectra in toluene show a band at  $1680\text{ cm}^{-1}$ , proving that a large proportion of the amides are not H-bonded, which is in contrast to the self-assemblies in  $C_6H_{12}$  where all the amides are H-bonded. Therefore toluene weakens the self-assembly, probably by interacting with BHPB-*n* through  $\pi$ - $\pi$  interactions. In addition, the ester band shows a major band at  $1710\text{ cm}^{-1}$  (a shouldering band is present at  $1724\text{ cm}^{-1}$  but with a much lower intensity) (Fig. 4). The structures of the self-assemblies of compounds BHPB-*n*, when  $n \geq 12$ , are shown in Fig. 8. They all exhibit ribbons with average widths varying from 56 nm to 25 nm (Table 1). Most of these ribbons tend to wind into tapes, with irregular helical turns along their main axis. No cylindrical structure was ever observed for these compounds.

To summarize, TEM shows that BHPB-*n* with  $n \geq 7$  form ribbons with limited width that tend to wind into helical or tubular shapes. BHPB-5 and 6 are the only compounds in the series forming truly flat ribbons. They also have a single ester  $\nu_{\text{CO}}$  band in their IR spectra, whereas all other compounds have two  $\nu_{\text{CO}}$  bands. This suggests that the tapes wind only when the esters in the constituting molecules have two different conformations or orientations. This hypothesis is also supported by the fact that in toluene, only flat ribbons form and, in conjunction, one of the ester  $\nu_{\text{CO}}$  peaks becomes predominant.

### Small angle scattering

TEM clearly proved the tubular shape of some aggregates and can provide an estimate of their outer diameter. But the inner and outer diameters can be measured more precisely only by small angle scattering techniques.<sup>22,42–47</sup> Therefore the

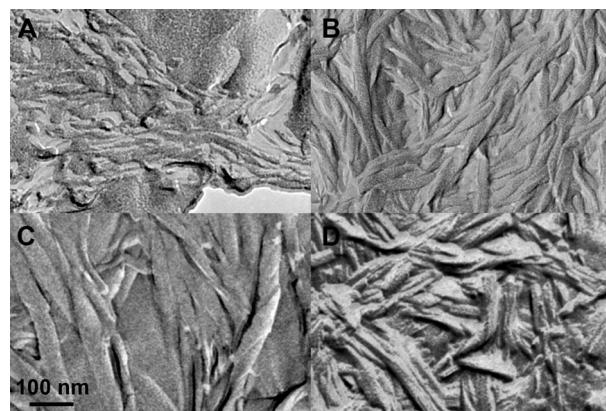


**Fig. 8** Freeze fracture TEM of (A) BHPB-13; (B) BHPB-14; (C) BHPB-15; (D) BHPB-16 in  $C_6H_{12}$  (2 wt%).

self-assemblies formed by compounds BHPB-8 to BHPB-12 were studied by SANS. They were prepared in deuterated solvent (1 wt% conc.) and subjected to a neutron beam. The intensities scattered by the self-assemblies were collected in a wide range of scattering vector  $q$  ( $0.0011 \text{ \AA}^{-1} < q < 0.64 \text{ \AA}^{-1}$ ). The corrected intensities were normalized to the Porod invariant  $Q$  (see Material and methods). The normalized intensities depend only on the geometrical parameters of the particles (eqn (4)).

**General overview of the normalized scattering cross sections.** The normalized scattering cross sections  $d\Sigma/d\Omega(q)/Q$  for the series of gelators are presented in Fig. 9.

BHPB-8, BHPB-9 and BHPB-10 exhibit very similar features: in the lowest  $q$  region ( $q < 0.01 \text{ \AA}^{-1}$ ), the normalized intensity varies as a power-law with an exponent between 1.5 and 2. No plateau is observed. If the scattering intensity is only due to uncorrelated particles, it indicates that the Guinier region is not reached with the experimental setup but is shifted to lower  $q$  values. This is consistent with very long particles as observed by electron microscopy experiments and validates the choice of an infinite cylinder form factor. Above  $0.01 \text{ \AA}^{-1}$ , we enter the asymptotic region (Porod region). The scattered intensity has an overall decrease in  $q^{-4}$ , characteristic of sharp interfaces. It also displays sharp oscillations, related to the cross-section of the fibrillar objects. Their positions move with the nature of the compounds and indicate a variation of the external radius for BHPB-8, BHPB-9 and BHPB-10. At higher  $q$ -values, a large oscillation is found at a common value (around  $0.25 \text{ \AA}^{-1}$  for the three compounds).

The form factor of long hollow cylinders (*e.g.* for which  $L \gg 10r_{\text{ext}}$ , with  $L$  the length of the nanotubes) can be written as

$$P(q, r_{\text{ext}}, e) = \frac{\pi}{qL} \left[ \frac{r_{\text{ext}} J_1(qr_{\text{ext}}) - (r_{\text{ext}} - e) J_1(q(r_{\text{ext}} - e))}{qe(r_{\text{ext}} - e/2)} \right]^2 \quad (5)$$

with  $r_{\text{ext}}$  the external radius of the tube,  $e$  the thickness of the wall and  $J_1$  the Bessel function of first kind and first order. This single tube model reproduces the main experimental features of the experimental curve (Fig. 10) on an absolute scale.

But compared with the theoretical curve, the experimental oscillations are attenuated, and for  $q > 0.25$ , reproduce only the

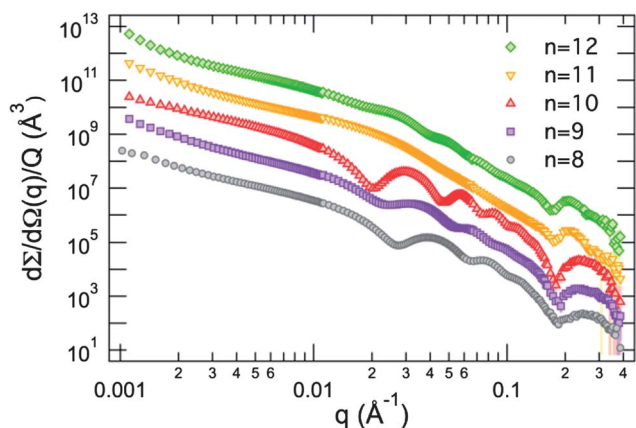


**Fig. 9** Normalized scattering cross sections  $d\Sigma/d\Omega(q)/Q$  for the BHPB- $n$  series. For the sake of clarity a vertical scaling offset ( $\times 10$ ) is applied to each curve except for BHPB-8.

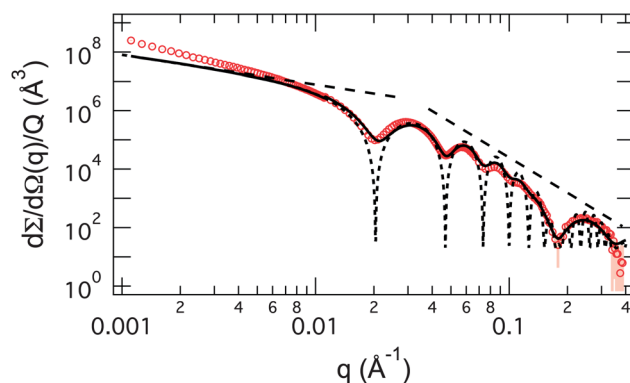


**Fig. 10**  $\circ$ : Experimental scattering cross section normalized to the Porod invariant (BHPB-10, 2% in  $\text{C}_6\text{D}_{12}$ ); dotted line: single infinite hollow cylinder model (eqn (4) and (5)) with  $r_{\text{ext}} = 13.5 \text{ nm}$ ,  $e = 3.5 \text{ nm}$ , scale factor = 1; solid line: same model with experimental resolution and radial distribution  $\Delta r = 0.68 \text{ nm}$  (eqn (4), (5) and (7)); dashed lines:  $q^{-1}$  and  $q^{-4}$  variation.

envelope curve of the fast theoretical oscillations. This deviation originates from the combination of finite experimental resolution and external radius polydispersity. The latter effect is more pronounced for BHPB-9 than for BHPB-8 and -10.

The resolution was calculated and applied to the fit as described in the Material and methods section. Radial polydispersity was taken into account by a symmetrical Gaussian distribution of the external radii  $g(r_{\text{ext}})$  (eqn (6)).

$$g(r_{\text{ext}}) = \frac{1}{\Delta r_{\text{ext}} \sqrt{2\pi}} \exp\left(-\frac{(r_{\text{ext}} - \bar{r}_{\text{ext}})^2}{\Delta r_{\text{ext}}^2}\right) \quad (6)$$

In this equation,  $\bar{r}_{\text{ext}}$  is the average external radius and  $\Delta r_{\text{ext}}$  the distribution width (or standard deviation). The polydispersity is defined as  $\Delta r_{\text{ext}}/\bar{r}_{\text{ext}}$ . The thickness  $e$  was kept constant and the normalised scattering cross section can then be written as

$$\frac{d\Sigma/d\Omega(q)}{Q} = \int_0^\infty V_{\text{P}}(r_{\text{ext}}) g(r_{\text{ext}}) P(q, r_{\text{ext}}) dr_{\text{ext}} \quad (7)$$

**Structural refinements.** Even when the resolution and radial polydispersity are taken into account, the intensity in the low  $q$  region (below  $5 \times 10^{-3} \text{ \AA}^{-1}$ ) is underestimated (Fig. 10). Moreover the positions of the first minima and maxima mismatch those of the best fits. The scaling exponent for low  $q$  is larger than unity, as it should be for uncorrelated cylinders. This intensity can be explained by the association of the tubes into clusters and can be modelled successfully by clusters of three tubes<sup>47</sup> and even simple pairs.<sup>28</sup> We have implemented the pair model in the present study. When two identical parallel tubes associate in close contact with a centre-to-centre distance  $2r_{\text{ext}}$ , the initial intensity (eqn (5)) has to be multiplied by the interference term:<sup>48</sup>

$$(1 + J_0(2qr_{\text{ext}})) \quad (8)$$

where  $J_0$  is the Bessel function of first kind and zero order. Therefore, the calculation was approximated by considering pairs of tubes with the same radius and by varying this radius

according to the distribution function  $g(r_{\text{ext}})$ . In the absence of correlation between pairs, eqn (4) is replaced by

$$\begin{aligned} \frac{d\Sigma/d\Omega(q)}{Q} &= \int_0^\infty V_P(r_{\text{ext}}) g(r_{\text{ext}}) P(q, r_{\text{ext}}) (1 + J_0(2qr_{\text{ext}})) dr_{\text{ext}} \\ &= \int_0^\infty V_P(r_{\text{ext}}) g(r_{\text{ext}}) P(q, r_{\text{ext}}) dr_{\text{ext}} \\ &\quad + \int_0^\infty V_P(r_{\text{ext}}) g(r_{\text{ext}}) P(q, r_{\text{ext}}) J_0(2qr_{\text{ext}}) dr_{\text{ext}} \quad (9) \end{aligned}$$

To calculate the exact intensity, we should consider pairs of cylinders with different diameters, derive their scattered intensity and then sum over all the pairs. But the simple eqn (8) holds only for identical cylinders and the exact intensity is more complicated to derive. The second term in eqn (9) represents the extra scattering contribution from the pairing. It exhibits a series of positive and negative oscillations at low  $q$  values and tends to 0 with increasing  $q$  values. These maxima/minima, restricted at low  $q$  values, alter the shape of the first oscillations (first term in eqn (9)). In addition, the association increases the intensity at low  $q$  values (both terms of eqn (8) are identical for sufficiently low  $q$ ). The  $q^{-1}$  behaviour is still present but is now shifted to smaller  $q$  values than for isolated nanotubes. Finally, solutions where only a fraction  $f_{\text{cluster}}$  of the tubes form clusters can be modelled simply by multiplying the second term in eqn (10) by  $f_{\text{cluster}}$ . Fig. 11 presents the best fit derived from eqn (9). For a better visualization, two other representations are shown:  $q^2 d\Sigma/d\Omega(q)/Q$  (Kratky plot, Fig. 11B) and  $q^4 d\Sigma/d\Omega(q)/Q$  (Porod representation, Fig. 11C).

The model reproduces quantitatively the normalized scattering cross section with a scale factor close to unity ( $scale = 0.95$ ). The presence of clusters greatly refines the fit below  $0.03 \text{ \AA}^{-1}$  where the experimental low  $q$  behavior and the shape of the first oscillation are reproduced more exactly. The same procedure was applied for BHPB-8 and -9 (Fig. 12).

The intensity scattered by BHPB-11 shows no oscillations and no simple geometric model can reproduce the data. These observations are consistent with the irregular and helical tapes with different diameters or widths observed by TEM for BHPB-11. No attempt was made to fit the data with a more sophisticated model. The scattering pattern observed for BHPB-12 is very close to that of BHPB-11, especially with a similar Bragg contribution around  $0.2 \text{ \AA}^{-1}$ . But it also shows attenuated oscillations, too weak to be modelled by tubes even with a large external radius polydispersity. This feature results from the mixture of particles of different shapes (tapes and nanotubes) and cannot be addressed by our model although well-defined nanotubes are clearly present.

A more accurate inspection needs to separate the different contributions. Since the scattering cross sections of BHPB-11 and BHPB-12 are very similar, we have assumed that the tapes present in BHPB-12 gels are the same as those in BHPB-11 gels. The scattering of BHPB-11 was treated as the contribution of the tapes in BHPB-12. Thus, we removed a fraction  $f_{\text{BHPB-11}}$  of  $d\Sigma_{\text{BHPB-11}}/d\Omega/Q$  from  $d\Sigma_{\text{BHPB-12}}/d\Omega/Q$  to enhance the contribution of the sole tubes. The result was multiplied by

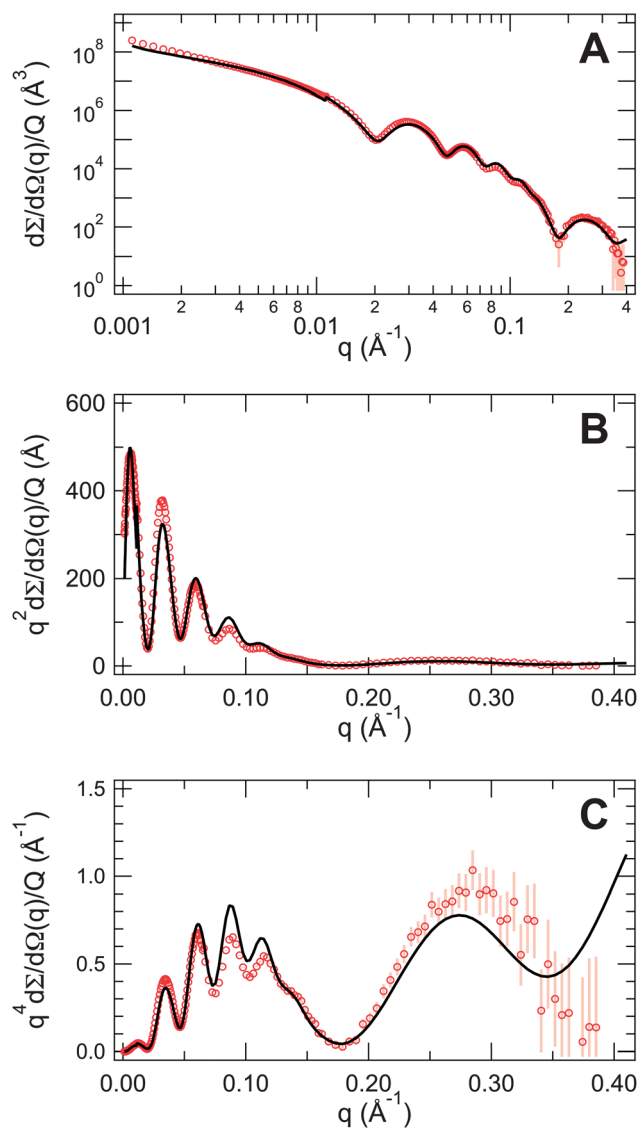


**Fig. 11** Structural refinement of BHPB-10 using the cluster model of eqn (9) (solid line). (A) Logarithmic; (B) Kratky; (C) Porod representations.

$1/(1 - f_{\text{BHPB-11}})$  to renormalize correctly to the modified Porod invariant. The resulting scattering cross section (Fig. 12,  $n = 12^*$ ) becomes very similar to that of the other samples and can be fitted with a single hollow cylinder model below  $0.05 \text{ \AA}^{-1}$ .

For higher  $q$  values, the refinement has a lower quality than for the other compounds but the subtraction allows the extraction of the first oscillations and a good estimate of the parameters of the tubes in the mixture. We also note that the Bragg peak is still present around  $0.2 \text{ \AA}^{-1}$  and partially masks the large oscillation around  $0.25 \text{ \AA}^{-1}$ . The intensity of BHPB-9 was treated by the same procedure as BHPB-12, the subtraction of  $d\Sigma_{\text{BHPB-11}}/d\Omega(q)/Q$ , but with a smaller  $f_{\text{BHPB-11}}$  fraction. This treatment enhanced the first minimum around  $0.02 \text{ \AA}^{-1}$  with a better definition. Fig. 12 presents the best fits for the series of self-assemblies. Final parameters are reported in Table 2. All the fits in different representations (log-log, Kratky and Porod) are presented in the ESI.†

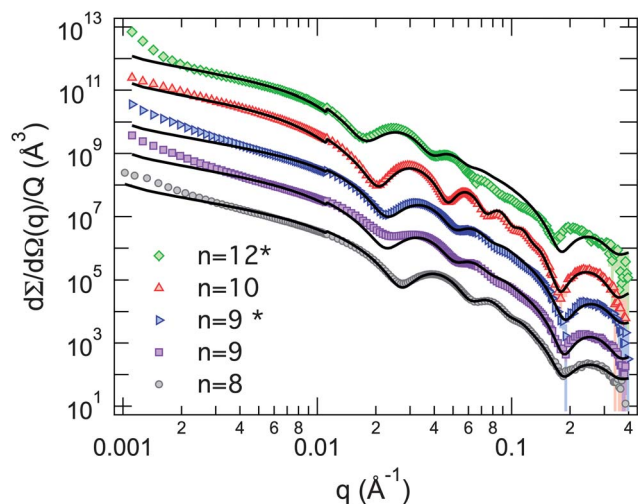


**Fig. 12** Best fits (solid lines) for the series of gelators BHPB- $n$ . Samples for which a fraction of  $d\Sigma_{\text{BHPB-11}}/d\Omega(q)/Q$  has been removed are indicated with an asterisk. A vertical scaling offset ( $\times 10$ ) is applied to each curve except for BHPB-8.

The thickness of the wall of the nanotubes is constant within the uncertainty of the measurements when  $n$  varies. The found distances 3.4 to 3.5 nm correspond to the lengths of the molecules in extended conformations. A monolayer could fit within this wall thickness, but more complex models cannot be ruled out.

The evolution of the external diameter with the ester chain length  $n$  is plotted in Fig. 13A. This curve shows a strong correlation between the size of the ester and the radii of the tubes.

The polydispersity of the tubes (Fig. 13B) reaches its smallest for BHPB-10 (about 5%). BHPB-8 forms tubes with a higher radial polydispersity, but no subtraction was necessary to implement the model, which proves that only tubes are present in the mixture. BHPB-9 forms tubes with about the same polydispersity as BHPB-8; however, intensities scattered by BHPB-9 have attenuated oscillations that have been modelled by the presence of non-tubular objects in the mixtures. The quality of the self-assembled nanotubes follows the order BHPB-10  $>$  8  $>$  9  $>$  12  $\gg$  11. The length of 10 C is thus the optimal value, yielding tubes with the lowest dispersity. For this length, the fraction of paired tubes is also higher than for BHPB-8 or 9,

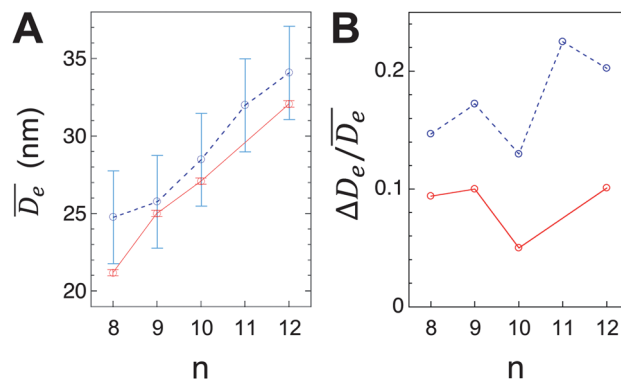


**Fig. 13** (A) Average external diameter  $\overline{D}_e$  of the tubes vs.  $n$ ; (B) polydispersity of the tube diameters vs.  $n$ . Solid line: measured by SANS. Dashed line: measured by TEM.

which suggests that a lower diameter polydispersity tends to favor the alignment of the tubes.

## Conclusions

We have studied a family of ester-diamide compounds that are organogelators at low concentration. We have identified the length of the ester chain ( $n$ ) as the molecular parameter that governs the shape of the self-assemblies. When this length is below a given threshold ( $n \leq 7$ ), the self-assemblies are flat ribbons, and when the length is above ( $n \geq 8$ ) the ribbons tend to wind into irregular helical tapes. For lengths between 8 and 10 C, the self-assemblies are mainly nanotubes with a well-defined shape, and for the length of 12 C, they self-assemble into more polydisperse tubes along with a majority of helical tapes. The scattering methods and the models we proposed successfully provide the diameter distribution and the wall thickness of the tubes. They also yield an estimate of the ratio of paired tubes and the proportion of non-tubular objects that may eventually co-exist with these tubes. An ester length of 10 C produces tubes with the lowest diameter polydispersity. A slight variation of this length yields nanotubes with varying diameters and with a broader distribution. FTIR and DSC studies show that the H-bonds between the amide groups are the main interactions driving the self-assemblies. Additionally, FTIR also proves the involvement of the ester groups. Whenever the

**Table 2** Parameters from the best fits for the series BHPB-8 to BHPB-12

Compound	BHPB-8	BHPB-9	BHPB-9, <sup>a</sup>		BHPB-12, <sup>a</sup>	
			$f_{\text{BHPB-11}} = 0.19$	BHPB-10	BHPB-10	$f_{\text{BHPB-11}} = 0.64$
Average external radius (nm)	$10.58 \pm 0.1$	$12.50 \pm 0.1$	$12.50 \pm 0.1$	$13.54 \pm 0.1$	$16.03 \pm 0.2$	$16.03 \pm 0.2$
Standard deviation $r_{\text{ext}}$ (nm)	$1.00 \pm 0.05$	$1.35 \pm 0.05$	$1.25 \pm 0.05$	$0.68 \pm 0.05$	$1.63 \pm 0.1$	$1.63 \pm 0.1$
$\Delta r_{\text{ext}}/\overline{r_{\text{ext}}}$	0.094	0.108	0.100	0.050	0.101	0.101
Thickness of the wall $e$ (nm)	$3.4 \pm 0.1$	$3.4 \pm 0.1$	$3.35 \pm 0.1$	$3.55 \pm 0.1$	$3.5 \pm 0.2$	$3.5 \pm 0.2$
Fraction of tubes in clusters $f_{\text{cluster}}$	0.4	0.3	0	0.8	0	0
Scale factor	0.96	0.88	0.95	0.96	1.06	1.06
Background bkg <sup>b</sup> ( $\text{\AA}^3$ )	70	30	40	25	60	60

<sup>a</sup> Sample for which a fraction of  $d\Sigma_{\text{BHPB-11}}/d\Omega(q)/Q$  has been removed;  $f_{\text{BHPB-11}}$ : corresponding removed fraction. <sup>b</sup> See Experimental.

aggregates are curved, *i.e.* if they are either helical tapes or tubes, their IR signature involves two ester bands suggesting two different sets of molecules in the self-assemblies. Efforts to elucidate the inner structure will be pursued by studies on oriented samples.

## Acknowledgements

This work was supported by two fellowships from the Région Alsace (T. T. N. and F.-X. S.), one fellowship from the Mexican CONACyT (N. D.) and by a grant from the International Center for Frontier Research in Chemistry, Strasbourg.

## Notes and references

- 1 T. Shimizu, M. Masuda and H. Minamikawa, *Chem. Rev.*, 2005, **105**, 1401–1443.
- 2 S. Vauthey, S. Santoso, H. Gong, N. Watson and S. Zhang, *Proc. Natl. Acad. Sci. U. S. A.*, 2002, **99**, 5355–5360.
- 3 E. M. Wilson-Kubalek, R. E. Brown, H. Celia and R. A. Milligan, *Proc. Natl. Acad. Sci. U. S. A.*, 1998, **95**, 8040–8045.
- 4 P. Ringler, W. Muller, H. Ringsdorf and A. Brisson, *Chem.–Eur. J.*, 1997, **3**, 620–625.
- 5 P. Huetz, S. van Neuren, P. Ringler, F. Kremer, J. F. L. van Breemen, A. Wagenaar, J. B. F. N. Engberts, J. G. E. M. Fraaije and A. Brisson, *Chem. Phys. Lipids*, 1997, **89**, 15–30.
- 6 Y. Ono, K. Nakashima, M. Sano, Y. Kanekiyo, K. Inoue, J. Hojo and S. Shinkai, *Chem. Commun.*, 1998, 1477–1478.
- 7 J. H. Jung, Y. Ono, K. Hanabusa and S. Shinkai, *J. Am. Chem. Soc.*, 2000, **122**, 5008–5009.
- 8 J. H. Jung, S.-H. Lee, J. S. Yoo, K. Yoshida, T. Shimizu and S. Shinkai, *Chem.–Eur. J.*, 2003, **9**, 5307–5313.
- 9 F. X. Simon, N. S. Khelfallah, M. Schmutz, N. Diaz and P. J. Mesini, *J. Am. Chem. Soc.*, 2007, **129**, 3788–3789.
- 10 W. Helfrich, *J. Chem. Phys.*, 1986, **85**, 1085–1087.
- 11 U. Seifert, J. Shillcock and P. Nelson, *Phys. Rev. Lett.*, 1996, **77**, 5237.
- 12 J. V. Selinger and J. M. Schnur, *Phys. Rev. Lett.*, 1993, **71**, 4091.
- 13 J. V. Selinger, M. S. Spector and J. M. Schnur, *J. Phys. Chem. B*, 2001, **105**, 7157–7169.
- 14 J. V. Selinger, F. C. MacKintosh and J. M. Schnur, *Phys. Rev. E: Stat. Phys., Plasmas, Fluids, Relat. Interdiscip. Top.*, 1996, **53**, 3804–3818.
- 15 C. M. Chen, *Phys. Rev. E: Stat. Phys., Plasmas, Fluids, Relat. Interdiscip. Top.*, 1999, **59**, 6192–6195.
- 16 D. S. Chung, G. B. Benedek, F. M. Konikoff and J. M. Donovan, *Proc. Natl. Acad. Sci. U. S. A.*, 1993, **90**, 11341–11345.
- 17 W. Helfrich and J. Prost, *Phys. Rev. A: At., Mol., Opt. Phys.*, 1988, **38**, 3065–3068.
- 18 R. Oda, I. Huc, M. Schmutz, S. J. Candau and F. C. MacKintosh, *Nature*, 1999, **399**, 566–569.
- 19 S. B. Lee, R. Koepsel, D. B. Stolz, H. E. Warriner and A. J. Russell, *J. Am. Chem. Soc.*, 2004, **126**, 13400–13405.
- 20 A. Singh, P. E. Schoen and J. M. Schnur, *J. Chem. Soc., Chem. Commun.*, 1988, 1222–1223.
- 21 R. Oda, F. Artzner, M. Laguerre and I. Huc, *J. Am. Chem. Soc.*, 2008, **130**, 14705–14712.
- 22 C. Valery, M. Paternostre, B. Robert, T. Gulik-Krzywicki, T. Narayanan, J. C. Dedieu, G. Keller, M. L. Torres, R. Cherif-Cheikh, P. Calvo and F. Artzner, *Proc. Natl. Acad. Sci. U. S. A.*, 2003, **100**, 10258–10262.
- 23 A. Brizard, C. Aime, T. Labrot, I. Huc, D. Berthier, F. Artzner, B. Desbat and R. Oda, *J. Am. Chem. Soc.*, 2007, **129**, 3754–3762.
- 24 M. Masuda and T. Shimizu, *Langmuir*, 2004, **20**, 5969–5977.
- 25 B. N. Thomas, C. M. Lindemann, R. C. Corcoran, C. L. Cotant, J. E. Kirsch and P. J. Persichini, *J. Am. Chem. Soc.*, 2002, **124**, 1227–1233.
- 26 C. Tarabout, S. Roux, F. Gobeaux, N. Fay, E. Pouget, C. Meriadec, M. Ligeti, D. Thomas, M. IJsselstijn, F. Besselièvre, D.-A. Buisson, J.-M. Verbavatz, M. Petitjean, C. Valéry, L. Perrin, B. Rousseau, F. Artzner, M. Paternostre and J.-C. Cintrat, *Proc. Natl. Acad. Sci. U. S. A.*, 2011, **108**, 7679–7684.
- 27 N. Diaz, F. X. Simon, M. Schmutz, M. Rawiso, G. Decher, J. Jestin and P. J. Mésini, *Angew. Chem., Int. Ed.*, 2005, **44**, 3260–3264.
- 28 T.-T.-T. Nguyen, F.-X. Simon, J. Combet, M. Schmutz and P. J. Mésini, *Soft Matter*, 2011, **7**, 1121–1128.
- 29 J. S. Pedersen, *J. Phys. IV*, 1993, **03**, 491–498.
- 30 I. Grillo, in *Small-angle neutron scattering and applications in soft and condensed matter*, ed. R. Borsali and R. Pecora, Springer-Verlag, Heidelberg, 2008, pp. 3–60.
- 31 S. Kline, *J. Appl. Crystallogr.*, 2006, **39**, 895–900.
- 32 P. Terech and R. G. Weiss, *Chem. Rev.*, 1997, **97**, 3133–3159; R. G. Weiss and P. Terech, *Molecular gels. Materials with self-assembled Fibrillar Network*, Springer, Dordrecht, The Netherlands, 2006; *Low Molecular Mass Gelator - Design, Self-Assembly, Function, Top. Curr. Chem.*, ed. F. Fages, 2005, vol. 256; M.-O. M. Piepenbrock, G. O. Lloyd, N. Clarke and J. W. Steed, *Chem. Rev.*, 2009, **110**, 1960–2004; A. Dawn, T. Shiraki, S. Haraguchi, S.-I. Tamaru and S. Shinkai, *Chem.–Asian J.*, 2011, **6**, 266–282.
- 33 F. W. Billmeyer Jr, *J. Appl. Phys.*, 2004, **28**, 1114.
- 34 P. J. Flory and A. Vrij, *J. Am. Chem. Soc.*, 1963, **85**, 3548–3553.
- 35 B. Wunderlich and G. Czornyj, *Macromolecules*, 1977, **10**, 906–913.
- 36 M. Davies and D. K. Thomas, *J. Phys. Chem.*, 1956, **60**, 767–770.
- 37 M. Schmutz and P. J. Mésini, in *Handbook of Cryopreparation Methods for Electron Microscopy*, ed. A. Cavalier, D. Spehner and B. M. Humbel, Francis and Taylor CRC Press, New York, 2008, pp. 411–430.
- 38 R. Schmidt, F. B. Adam, M. Michel, M. Schmutz, G. Decher and P. J. Mésini, *Tetrahedron Lett.*, 2003, **44**, 3171–3174.
- 39 R. Schmidt, M. Schmutz, M. Michel, G. Decher and P. J. Mésini, *Langmuir*, 2002, **18**, 5668–5672.
- 40 G. Palui, F.-X. Simon, M. Schmutz, P. J. Mésini and A. Banerjee, *Tetrahedron*, 2008, **64**, 175–185.

- 41 N. Nakashima, S. Asakuma and T. Kunitake, *J. Am. Chem. Soc.*, 1985, **107**, 509–510.
- 42 C. V. Teixeira, H. Amenitsch, T. Fukushima, J. P. Hill, W. Jin, T. Aida, M. Hotokka and M. Linden, *J. Appl. Crystallogr.*, 2010, **43**, 850–857.
- 43 P. Terech, A. De Geyer, B. Struth and Y. Talmon, *Adv. Mater.*, 2002, **14**, 495–498.
- 44 P. Terech and Y. Talmon, *Langmuir*, 2002, **18**, 7240–7244.
- 45 T. Imae, K. Funayama, M. P. Krafft, F. Giulieri, T. Tada and T. Matsumoto, *J. Colloid Interface Sci.*, 1999, **212**, 330–337.
- 46 K. Sakurai, Y. Ono, J. H. Jung, S. Okamoto, S. Sakurai and S. Shinkai, *J. Chem. Soc., Perkin Trans. 2*, 2001, 108–112.
- 47 D. Dasgupta, Z. Kamar, C. Rochas, M. Dahmani, P. Mesini and J. M. Guenet, *Soft Matter*, 2010, **6**, 3573–3581.
- 48 G. Oster and D. P. Riley, *Acta Crystallogr.*, 1952, **5**, 272–276.